Built-in electric field and strain tunable valley-related multiple topological phase transitions in VSiXN$_4$ (X = C, Si, Ge, Sn, Pb) monolayers

Ping Li,[1,2,*] Xiao Yang,[3] Qing-Song Jiang,[3] Yin-Zhong Wu,[4,†] and Wei Xun[3,‡]

[1]*State Key Laboratory for Mechanical Behavior of Materials, Center for Spintronics and Quantum System, School of Materials Science and Engineering, Xi'an Jiaotong University, Xi'an, Shaanxi 710049, China*

[2]*State Key Laboratory for Surface Physics and Department of Physics, Fudan University, Shanghai 200433, China*

[3]*Faculty of Electronic Information Engineering, Huaiyin Institute of Technology, Huaian 223003, China*

[4]*School of Physical Science and Technology, Suzhou University of Science and Technology, Suzhou 215009, China*

(Received 15 October 2022; revised 13 April 2023; accepted 22 May 2023; published 7 June 2023)

Valley-related multiple topological phase transitions have attracted significant attention because they provide significant opportunities for fundamental research and practical applications. Unfortunately, however, there is no real material as of yet that can realize valley-related multiple topological phase transitions. Here, through first-principles calculations and model analysis, we investigate the structural, magnetic, electronic, and topological properties of VSiXN$_4$ (X = C, Si, Ge, Sn, Pb) monolayers. VSiXN$_4$ monolayers are stable and intrinsically ferrovalley materials. Intriguingly, we found that built-in electric field and strain can induce valley-related multiple topological phase transitions in materials from valley semiconductor to valley half-semimetal, to valley quantum anomalous Hall insulator, to valley half-semimetal, and to valley semiconductor (or to valley metal). The nature of the topological phase transition is the built-in electric field and strain-induced band inversion between the $d_{xy}/d_{x^2-y^2}$ and d_{z^2} orbitals at K and K' valleys. Our findings not only reveal the mechanism of multiple topological phase transitions, but they also provide an ideal platform for the multifield manipulating the spin, valley, and topological physics. This will lead to alternative perspectives for spintronic, valleytronic, and topological nanoelectronic applications based on these materials.

DOI: 10.1103/PhysRevMaterials.7.064002

I. INTRODUCTION

Valley degrees of freedom and related manipulations have become rising topics in recent years [1,2]. They are coupled with the spin degree of freedom to exhibit extraordinary quantum effects [3–7], such as the valley spin Hall effect [8,9] and the valley polarized quantum anomalous Hall effect (VQAHE) [4,5,10–12]. The coupling effects are typically strong in the transition-metal elements with localized d electrons, and the effects will be further enhanced with a decrease of dimensions. Therefore, two-dimensional (2D) transition-metal materials provide a good opportunity to investigate the manifestation of charge, spin, topological, and valley quantum covariation effects.

In 2D hexagonal lattice material, the extreme value of the valence and conduction bands appears at the K and K' points, forming the valley degrees of freedom. Due to the effect of inversion symmetry ($\hat{P}$) breaking together with spin-orbit coupling (SOC), the K and K' valleys have opposite spins but degenerate energies, which is known as spin-valley locking. As a result, the charged carriers in the two opposite valleys were selectively stimulated by the photons with left-hand and right-hand circular polarization. In addition, if the system further breaks time-reversal symmetry ($\hat{T}$), the valley degenerate will disappear at the K and K' points. This is known as a ferrovalley [13]. Therefore, exploring ferrovalley materials is beneficial to promoting the development of spintronics and valleytronics.

Recently, a new 2D transition-metal material $MoSi_2N_4$ family was successfully synthesized in an experiment [14], and more than 60 stable ternary compounds with similar structures have been predicted theoretically [15]. Such a family of materials has many interesting physical properties, including intrinsic magnetism, valley polarization, transport, and topology [16–20]. It was noticed that 2D Janus transition-metal dichalcogenides (TMDs) were also experimentally synthesized [21]. It is well known that the $MoSi_2N_4$ family is a combination of TMDs and SiN surface layers. Therefore, we are optimistic that the Janus $MoSi_2N_4$ family can also be prepared. The two chalcogen layers are different, and the mirror symmetry in the Janus $MoSi_2N_4$ family is broken. The impact of spontaneous out-of-plane dipole (the built-in electric field) and strain on the covariation effect (charge, spin, topological, and valley) may be crucial, but it is not yet clearly understood.

In this work, we systematically investigate the built-in electric field and strain on the covariation effect of spin, topological, and valley freedom of VSiXN$_4$ (X = C, Si, Ge, Sn, Pb) monolayers. It is found that the built-in electric field and strain effects can induce a series of topological phase transitions, such as valley semiconductor (VSC), valley half-semimetal (VHSM), valley quantum anomalous Hall insulator (VQAHI), and valley metal (VM). It essentially originated from the built-in electric field and strain-induced

*pli@xjtu.edu.cn
†yzwu@usts.edu.cn
‡xunwei@hyit.edu.cn

band inversion between the $d_{xy}/d_{x^2-y^2}$ and d_{z^2} orbitals at the K and K' valleys. Our findings pave the way for valley-related multiple topological phase transitions and further microelectronic devices with perfect valley, spin, and topology.

II. STRUCTURES AND COMPUTATIONAL METHODS

To explore the electronic and magnetic structures, we used the Vienna *Ab initio* Simulation Package (VASP) [22–24] within the framework of the density functional theory (DFT) for first-principles calculations. The exchange-correlation energy was described by the generalized gradient approximation (GGA) with the Perdew-Burke-Ernzerhof (PBE) functional [25]. The plane-wave basis with a kinetic energy cutoff of 500 eV was employed, and $17 \times 17 \times 1$ and $25 \times 25 \times 1$ Γ-centered k meshes were adopted for structural optimization and self-consistent calculations. A vacuum of 20 Å was set along the c-axis to avoid the interaction between the sheet and its periodic images. The total energy convergence criterion and the force were set to 10^{-7} eV and -0.001 eV/Å, respectively. To describe strongly correlated $3d$ electrons of V [13,26], the GGA + U method was applied. The Coulomb repulsion U was varied between 1 and 4 eV. To confirm the results, the calculations were also checked using the Heyd-Scuseria-Ernzerhof (HSE06) method. To investigate the dynamical stability, the phonon spectra were calculated using a finite displacement approach as implemented in the PHONOPY code [27]. The maximally localized Wannier functions (MLWFs) were employed to construct an effective tight-binding Hamiltonian to explore the Berry curvature, anomalous Hall conductivity (AHC), and edge states [28]. Using the calculated AHC, we performed the Berry curvature calculations using the formula

$$\sigma_{xy} = \mathrm{Ch}\frac{e^2}{h}, \tag{1}$$

$$\mathrm{Ch} = \frac{1}{2\pi}\int_{\mathrm{BZ}} d^2k\ \Omega(\mathbf{k}), \tag{2}$$

$$\Omega(\mathbf{k}) = -\sum_n f_n \sum_{n'\neq n} \frac{2\,\mathrm{Im}\langle\psi_{nk}|v_x|\psi_{n'k}\rangle\langle\psi_{n'k}|v_y|\psi_{nk}\rangle}{(E_{n'}-E_n)^2}, \tag{3}$$

where Ch is the Chern number, $\Omega(\mathbf{k})$ is the Berry curvature in reciprocal space, v_x and v_y are operator components along the x and y directions, and $f_n = 1$ for the occupied bands [29–31]. One can obtain the Chern number as well as AHC by integrating the Berry curvature in the entire Brillouin zone (BZ). Therefore, the edge states were calculated in a half-infinite boundary condition using the iterative Green's function method using the WANNIERTOOLS package [32].

III. RESULTS AND DISCUSSION

A. Structure and stability

The crystal structure of the VSiXN$_4$ monolayer is shown in Fig. 1(a). VSiXN$_4$ consists of septuple layers of N-Si-N-V-N-X-N, with atoms in each layer forming a 2D hexagonal lattice. Each V atom is coordinated with six N atoms, forming a trigonal prismatic configuration, and then this VN_2 layer is sandwiched by Si-N and X-N layers. The space group of VSiXN$_4$ is $P3m1$ (no. 156), and the space inversion symmetry

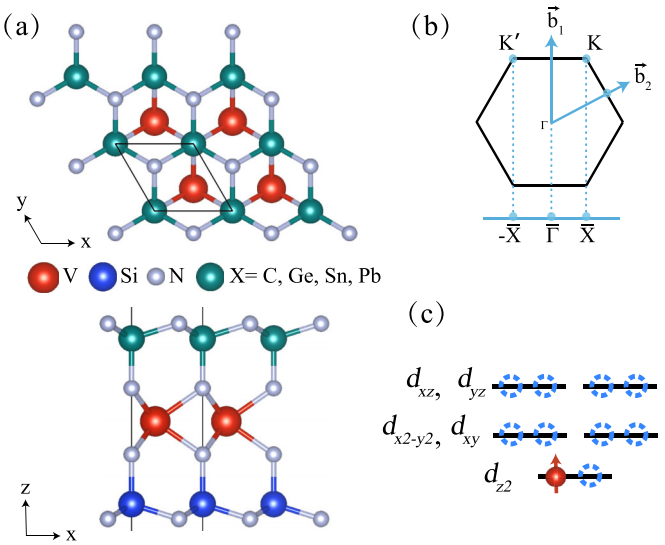

FIG. 1. (a) The top and side views of the crystal structure for VSiXN$_4$ (X = C, Si, Ge, Sn, Pb) monolayers. The red, gray, blue, and green balls represent V, N, Si, and X elements, respectively. (b) The Brillouin zone (BZ) of the honeycomb lattice with the reciprocal-lattice vectors $\vec{b}_1$ and $\vec{b}_2$. Γ, K, and M are the high-symmetry points in the BZ, and $\overline{\Gamma}$ and $\overline{X}$ are the high-symmetry points in the one-dimensional BZ. (c) The splitting of d orbitals under the trigonal prismatic crystal field.

is broken [except VSi_2N_4, which is P-6m2 (no. 187)]. The lattice constant of VSi_2N_4 is optimized to 2.88 Å, agreeing well with previous work [14,16]. However, the lattice constants of $VSiCN_4$, $VSiGeN_4$, $VSiSnN_4$, and $VSiPbN_4$ are optimized to 2.75, 2.95, 3.04, and 3.07 Å (see Table I), respectively. The lattice constant is increasing with the increase of the X atomic order. To confirm the stability of VSiXN$_4$ monolayers, the phonon spectra are calculated. As shown in Fig. S1, the absence of imaginary frequencies confirms that the VSiXN$_4$ monolayers are dynamically stable (see the supplemental material [33]). Only $VSiPbN_4$ has a small imaginary frequency at the Γ point, which is a numerical error. In previous reports [34,35], this is a common problem for 2D materials. These imaginary frequencies become smaller as we increase the supercell in the phonon spectrum calculations. In addition, as shown in Fig. S2, we calculated the formation energy for 2H and 1T phase VSiXN$_4$ [33]. The formation energy is

TABLE I. The calculated lattice constants a (Å) for the monolayer, magnetic anisotropy energy (MAE) (μeV/cell), the valley degeneracy splits for the valence [$E_v^K - E_v^{K'}$ (meV)] and conduction bands [$E_c^K - E_c^{K'}$ (meV)], and the global band gap E_g (meV) of the 2D material VSiXN$_4$ (X = C, Si, Ge, Sn, Pb).

	a	MAE	$E_v^K - E_v^{K'}$	$E_c^K - E_c^{K'}$	E_g
$VSiCN_4$	2.75	96.66	46.73	0.00	722.04
VSi_2N_4	2.88	50.98	63.74	0.00	381.33
$VSiGeN_4$	2.95	−4.16	70.17	0.00	0.00
$VSiSnN_4$	3.04	−17.41	0.00	68.86	118.91
$VSiPbN_4$	3.07	−30.27	0.00	72.45	0.00

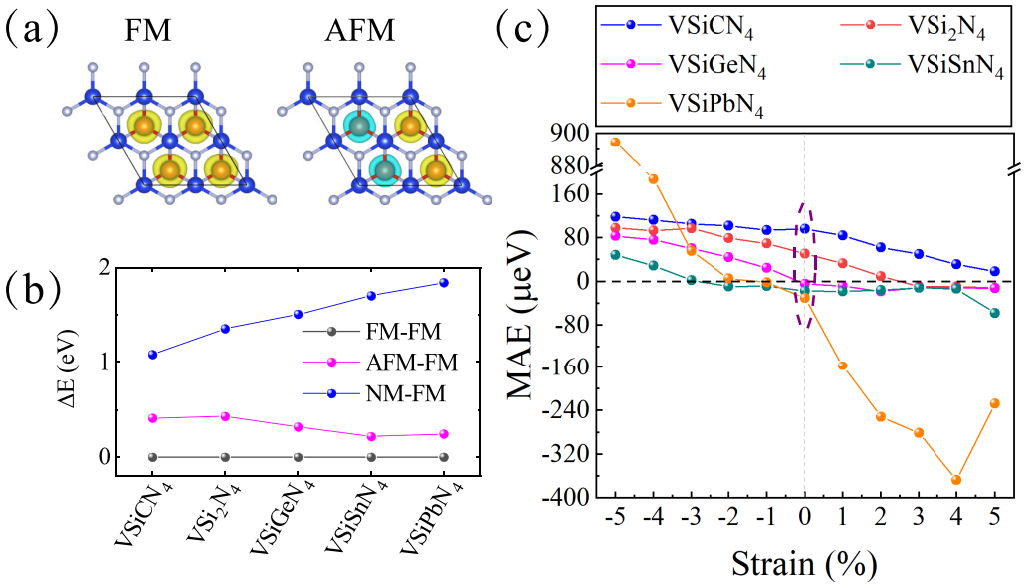

FIG. 2. (a) Spin charge densities with spin directions are indicated (yellow and cyan correspond to spin-up and spin-down, respectively). The isovalue surface level is at 0.005 $e/\text{Å}^3$. (b) Calculated total energies of VSiXN$_4$ different magnetic structures, which are defined relative to that of the FM state. (c) The magnetic anisotropy energy as a function of strain. These results were obtained with $U_{\text{eff}} = 3$ eV.

expressed as $E_f = (E_{\text{tot}} - \mu_{\text{V}} - \mu_X - 4\,\mu_{\text{N}})/N$, where E_{tot} is the total energy of VSiXN$_4$. μ_{V}, μ_X, and μ_{N} are the chemical potential V, X, and N atoms, respectively. N is the number of atoms in VSiXN$_4$. As listed in Table SI, the negative value, −6.390 to 7.504 eV, indicates that the VSiXN$_4$ lattice is a strongly bonded network and hence favors its experimental synthesis [33]. Even though the 1T phase formation energy of VSiGeN$_4$, VSiSnN$_4$, and VSiPbN$_4$ is lower than that of the 2H phase formation, the difference is very small. In addition, to confirm the dynamical stability of the 1T phase VSiXN$_4$, we calculated the phonon spectrum, as shown in Fig. S3 [33]. We found that the phonon spectrum of the 1T phase VSiXN$_4$ has a large imaginary frequency, which indicates that the dynamics of the 1T phase VSiXN$_4$ is unstable.

B. Magnetic property

The valence electron configuration of the V atom is $3d^3 4s^2$. After donating four electrons to the neighboring N atoms, one valence electron is retained. According to Hund's rule and the Pauli exclusion principle, the electron configuration of V^{4+} is split into three groups: a_1 (d_{z^2} orbital), e_1 (d_{xy}, $d_{x^2-y^2}$ orbital), and e_2 (d_{z^2} orbital), as shown in Fig. 1(c). Therefore, the magnetic moment of the VSiXN$_4$ monolayer is expected to be 1 μ_B per cell. Our spin-polarized calculations indeed show that VSiCN$_4$, VSi$_2$N$_4$, VSiGeN$_4$, and VSiSnN$_4$ are spin-polarized, and that the magnetic moments are mainly distributed over the V atoms, with a magnetic moment of 1 μ_B per unit. It is worth noting that only in VSiPbN$_4$ is the magnetic moment not 1 μ_B (it is 1.09 μ_B). Due to the increase of the out-of-plane dipole formed by Si and Pb atoms, VSiPbN$_4$ becomes a VM.

To determine the magnetic ground state of the VSiXN$_4$ monolayer, three possible magnetic configurations are considered, namely the ferromagnetic (FM), antiferromagnetic (AFM), and nonmagnetic (NM) structures [see Fig. 2(a)]. We calculate the total energy difference between FM, AFM, and NM using the GGA + U method. To determine a reasonable value of U, the GGA + U calculated energy difference between the AFM and FM states is compared with the HSE06 results, as shown in Fig. S4 [33]. It can be found that the value of U near 3 eV is consistent with the results of HSE06 for the VSiXN$_4$ monolayer. Therefore, we choose $U_{\text{eff}} = 3$ eV to investigate the VSiXN$_4$ (X = C, Si, Ge, Sn, Pb) system. By comparing the total energy of FM, AFM, and NM states, we found that the FM configuration is the magnetic ground state for the VSiXN$_4$ monolayer, as shown in Fig. 2(b). The FM ground state of the VSiXN$_4$ monolayer can be understood by studying the crystal structure. In VSiCN$_4$, VSiGeN$_4$, VSiSnN$_4$, and VSiPbN$_4$, the V-N-V bond angles are 87.9°, 91.4°, 92.8°, and 93.1°, respectively, which are close to 90.0°. According to the Goodenough-Kanamori-Anderson rule [36–38], this configuration is beneficial to FM coupling.

Then, we investigate the underlying physics for the robust out-of-plane magnetization. The direction of spin-polarization orientation is determined by magnetic anisotropy energy (MAE), which is defined as MAE = $E_z - E_{x/y}$. First, we tested the convergence of the K-mesh before calculating MAE. As shown in Fig. S5, when the K-mesh is 25 × 25 × 1, the convergence criterion is reached completely [33]. The MAE is calculated using 25 × 25 × 1 K-mesh in Fig. 2(c). The MAE value is listed in Table I. For magnetic ions V with a finite orbital moment, MAE can be estimated through the formula $\lambda\langle L\rangle\langle S\rangle$, where λ, L, and S represent the strength of SOC, orbital angular momentum, and spin angular momentum [39], respectively. For the VSiXN$_4$ monolayer, the half-filled a_1 and empty e_1, e_2 orbitals indicate that $L = 0$ and $S = 1/2$. Due to the quenched orbital moment, the MAE originating from the SOC of the V atom vanishes. As a result, MAE is mainly contributed by the SOC effect originating from N and X (X = C, Si, Ge, Sn, Pb) atoms. The MAE can be

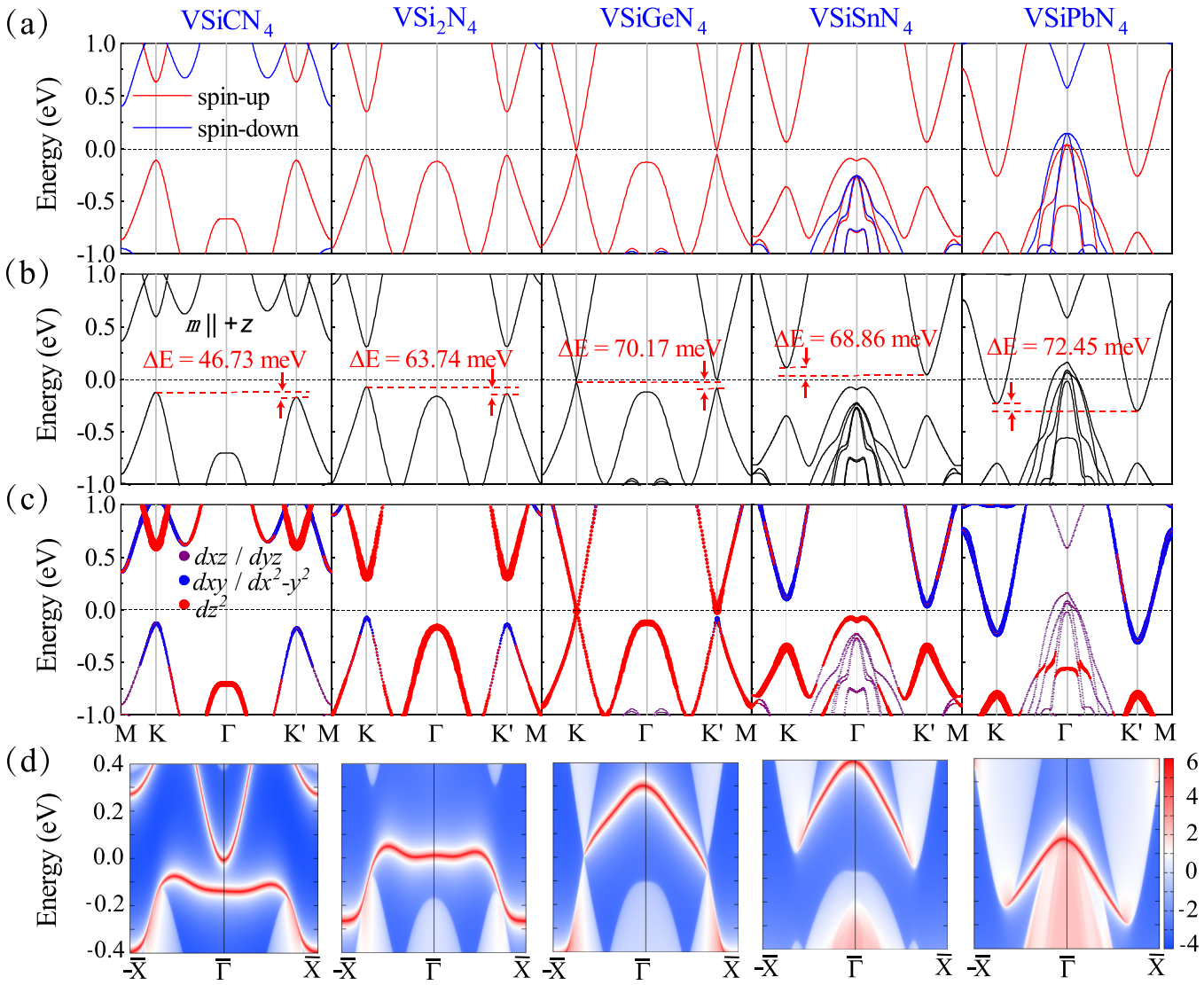

FIG. 3. Band structures and edge state of VSiXN$_4$ monolayer obtained with the GGA + U (U_{eff} = 3 eV) method. (a) Spin-polarized band structures of VSiXN$_4$ monolayer. The red and blue lines represent spin-up and spin-down bands, respectively. (b) Band structure with SOC of VSiXN$_4$ monolayer. (c) Orbital-resolved band structure with SOC of VSiXN$_4$ monolayer. (d) The edge state of VSiXN$_4$ monolayer.

written as [40–42]

$$\text{MAE} = \xi^2 \sum_{u,o,\sigma,\sigma'} \sigma\sigma' \frac{|\langle o,\sigma|L_z|u,\sigma'\rangle|^2 - |\langle o,\sigma|L_x|u,\sigma'\rangle|^2}{E_{u,\sigma} - E_{o,\sigma'}}, \tag{4}$$

where o and u denote the occupied and unoccupied states, respectively. The spin indices σ and σ' run over ± 1, amounting to each of the two orthogonal spin states at the K point. $E_{u,\sigma}$ and $E_{o,\sigma'}$ are the band energy of the states. As shown in Fig. S6, u and o are mainly contributed by N p_x and p_y orbitals. The contribution from the X (X = C, Si, Ge, Sn, Pb) atomic orbitals is almost negligible [33]. Therefore, u and o can be written as $a_\tau = a_x + i\tau a_y$ from V atoms and $p'_\tau = p_x + i\tau' p_y$ from N atoms, where $\tau = \pm 1$ and $\tau' = \pm 1$. Therefore, MAE can be simplified as

$$\text{MAE} = \xi^2 \sum_{\tau,\tau'} \frac{\left|\langle a_\tau|L_z^N|p_{\tau'}\rangle\right|^2 - \left|\langle a_\tau|L_x^N|p_{\tau'}\rangle\right|^2}{\Delta}, \tag{5}$$

where Δ is the band gap, $L_z|p_{\tau'}\rangle = \tau'|p_{\tau'}\rangle$ and $L_x|p_{\tau'}\rangle = i\tau'|p_z\rangle$, and

$$\text{MAE} = \xi^2 \sum_{\tau,\tau'} \frac{|\langle a_\tau|p_{\tau'}\rangle|^2 - |\langle a'_\tau|p_z\rangle|^2}{\Delta}. \tag{6}$$

The spin orientation is determined by the orbital overlaps of $\langle a_\tau|p_{\tau'}\rangle$ and $\langle a'_\tau|p_z\rangle$. In a purely octahedral crystal environment, the irreducible representations of the p'_τ and p_z of the ligands are $E_u \oplus E_g$ and $A_{1g} \oplus A_{2u}$, respectively. a_τ of V atoms belongs to E_g, which indicates that a_τ tends to couple with p'_τ instead of p_z from N atoms. Thus, $|\langle a_\tau|p_{\tau'}\rangle| \gg |\langle a'_\tau|p_z\rangle|$. This indicates that the MAE favors a positive value,

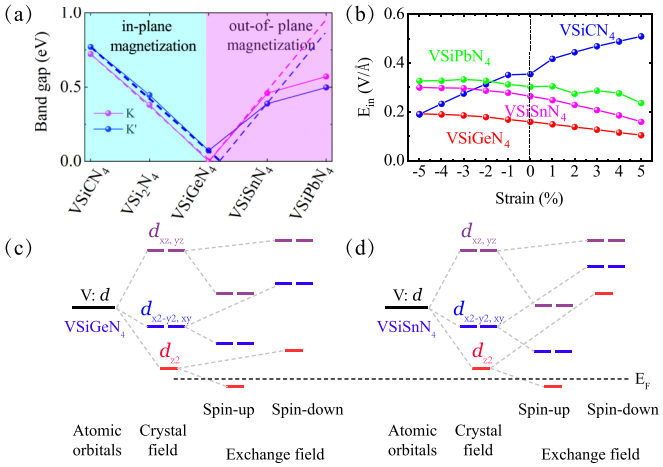

FIG. 4. (a) The band gap of VSiXN$_4$ (X = C, Si, Ge, Sn, Pb) at K and K' points. The dotted line is the fitting K and K' point gap variation trend. (b) The built-in electric field (E_{in}) as functions of strain for VSiXN$_4$ monolayer. (c),(d) The schematic illustration of energy level for V-d orbital in VSiGeN$_4$ (c) and VSiSnN$_4$ (d). E_F represents the Fermi level. These results were obtained with $U_{\text{eff}} = 3$ eV.

benefiting the out-of-plane spin orientation. In fact, VSiCN$_4$ and VSi$_2$N$_4$ have an easy magnetization plane, while the easy axes of VSiGeN$_4$, VSiSnN$_4$, and VSiPbN$_4$ are along the out-of-plane direction, as shown in Fig. 2(c). This is attributed to the fact that the MAE is tunable by the strong dipole interaction of the system. MAE is an intrinsic property of the material. There are many factors affecting the MAE of materials, such as spin-orbit coupling, structure, orbital occupation, and so on. In VSiXN$_4$, MAE is mainly determined by the built-in electric field. As shown in Fig. 4(b), in the absence of strain, the VSiCN$_4$ has the largest built-in electric field. In addition, the built-in electric field is 0.36 V/Å (VSiCN$_4$), 0.16 V/Å (VSiGeN$_4$), 0.26 V/Å (VSiSnN$_4$), and 0.31 V/Å (VSiPbN$_4$), respectively. To be precise, the MAE is 96.66 μeV (VSiCN$_4$), −4.16 μeV (VSiGeN$_4$), −17.41 μeV (VSiSnN$_4$), and −30.27 μeV (VSiPbN$_4$), respectively. The variation law of MAE is completely consistent with that of the built-in electric field. In addition, as shown in Fig. 2(c), we found that the tensile strain favors an out-of-plane magnetism. This is because the tensile strains reduce the distance between Si and X atoms, thus enhancing the dipole interactions.

C. Electronic band structure

In addition, we first calculated the band structure of VSiXN$_4$ with spin polarization but without SOC. As shown in Fig. 3(a), it can be found that there is a valley at each of the K and K' points. Both the valence and conduction bands of the valleys are spin-up bands. The two valleys are degenerate in energy. More interestingly, as the atomic number of X increases, it exhibits abundant electronic structure properties. VSiCN$_4$, VSi$_2$N$_4$, and VSiSnN$_4$ are VSC, while VSiGeN$_4$ and VSiPbN$_4$ are VHSM and VM, respectively. So we further calculated the band structures with the SOC effect. As shown in Figs. 3(b) and 3(c), it can be found that the valence-band valley of K is appreciably higher than K' for VSiCN$_4$, VSi$_2$N$_4$, and VSiGeN$_4$, while the conduction-band valley of K is obviously lower than K' for VSiSnN$_4$. Therefore, the valley degeneracy is broken, and an evident valley splitting $E_v^K - E_v^{K'}$ or $E_c^K - E_c^{K'}$ is induced. $E_v^K - E_v^{K'}$ (or $E_c^K - E_c^{K'}$) is 46.73, 63.74, 70.17, 68.86, and 72.45 meV for VSiCN$_4$, VSi$_2$N$_4$, VSiGeN$_4$, VSiSnN$_4$, and VSnPbN$_4$, respectively (see Table I).

Here, we highlight a novel phenomenon. The valley polarization of VSiCN$_4$, VSi$_2$N$_4$, and VSiGeN$_4$ only appears at the valence band, while it degenerates at the conduction band. On the contrary, the valley splitting of VSiSnN$_4$ and VSiPbN$_4$ occurs at the conduction band. It is important that VSiGeN$_4$ is the critical state, and the valence-band maximum (VBM) and conduction-band minimum (CBM) reveal degeneracy at the K point forming a Dirac cone. From the orbital-resolved band structure, as shown in Fig. 3(c), the VBM bands of VSiCN$_4$, VSi$_2$N$_4$, and VSiGeN$_4$ are mainly contributed by V $d_{xy}/d_{x^2-y^2}$ orbitals, while the CBM bands are dominated by d_{z^2} orbitals of the V atom. For VSiSnN$_4$ and VSiPbN$_4$ monolayer, on the contrary, the VBM bands are primarily d_{z2} orbital, while the CBM bands are mainly $d_{xy}/d_{x^2-y^2}$ orbitals. It can be found that the atomic number of the X atom induced band inversion between the $d_{xy}/d_{x^2-y^2}$ and d_{z2} orbitals. As is well known, the orbital angular momentum of the d_{z^2} orbital is zero. Therefore, the d_{z^2} orbital does not cause valley splitting. Notably, these results yield a good comparison with the band structures obtained from the HSE06 method, as shown in Fig. S7 [33].

To understand the underlying mechanism for the ferrovalley effect in VSiXN$_4$, we take VSiGeN$_4$ here as an example to perform model analysis. We adopted $|\psi_v^\tau\rangle = \frac{1}{\sqrt{2}}(|d_{xy}\rangle + i\tau|d_{x^2-y^2}\rangle) \otimes |\uparrow\rangle$, $|\psi_c^\tau\rangle = (|d_{z2}\rangle) \otimes |\uparrow\rangle$ as the orbital basis for the VBM and CBM, where $\tau = \pm 1$ indicate the valley index corresponding to K/K'. Since the VBM and CBM belong to the same spin channel (spin-up bands), we take the SOC effect as the perturbation term, which is

$$\hat{H}_{\text{SOC}} = \lambda \hat{S} \cdot \hat{L} = \hat{H}^0_{\text{SOC}} + \hat{H}^1_{\text{SOC}}, \tag{7}$$

where $\hat{S}$ and $\hat{L}$ are spin angular and orbital angular operators, respectively. $\hat{H}^0_{\text{SOC}}$ and $\hat{H}^1_{\text{SOC}}$ represent the interaction between the same spin states and between opposite spin states, respectively. For the VSiGeN$_4$ monolayer, the single valley is composed of only one spin channel [see Fig. 3(a)], and the other spin channel is far from the valleys. Hence, the term $\hat{H}^1_{\text{SOC}}$ can be ignored. On the other hand, $\hat{H}^0_{\text{SOC}}$ can be written in polar angles,

$$\hat{H}^0_{\text{SOC}} = \lambda \hat{S}_{z'}\left(\hat{L}_z \cos\theta + \frac{1}{2}\hat{L}_+ e^{-i\phi}\sin\theta + \frac{1}{2}\hat{L}_- e^{+i\phi}\sin\theta\right). \tag{8}$$

In the out-of-plane magnetization case, $\theta = \phi = 0$, the $\hat{H}^0_{\text{SOC}}$ term can then be simplified as

$$\hat{H}^0_{\text{SOC}} = \lambda \hat{S}_z \hat{L}_z. \tag{9}$$

The energy levels of the valleys for the VBM and CBM can be expressed as $E_v^\tau = \langle\psi_v^\tau|\hat{H}^0_{\text{SOC}}|\psi_v^\tau\rangle$ and $E_c^\tau = \langle\psi_c^\tau|\hat{H}^0_{\text{SOC}}|\psi_c^\tau\rangle$,

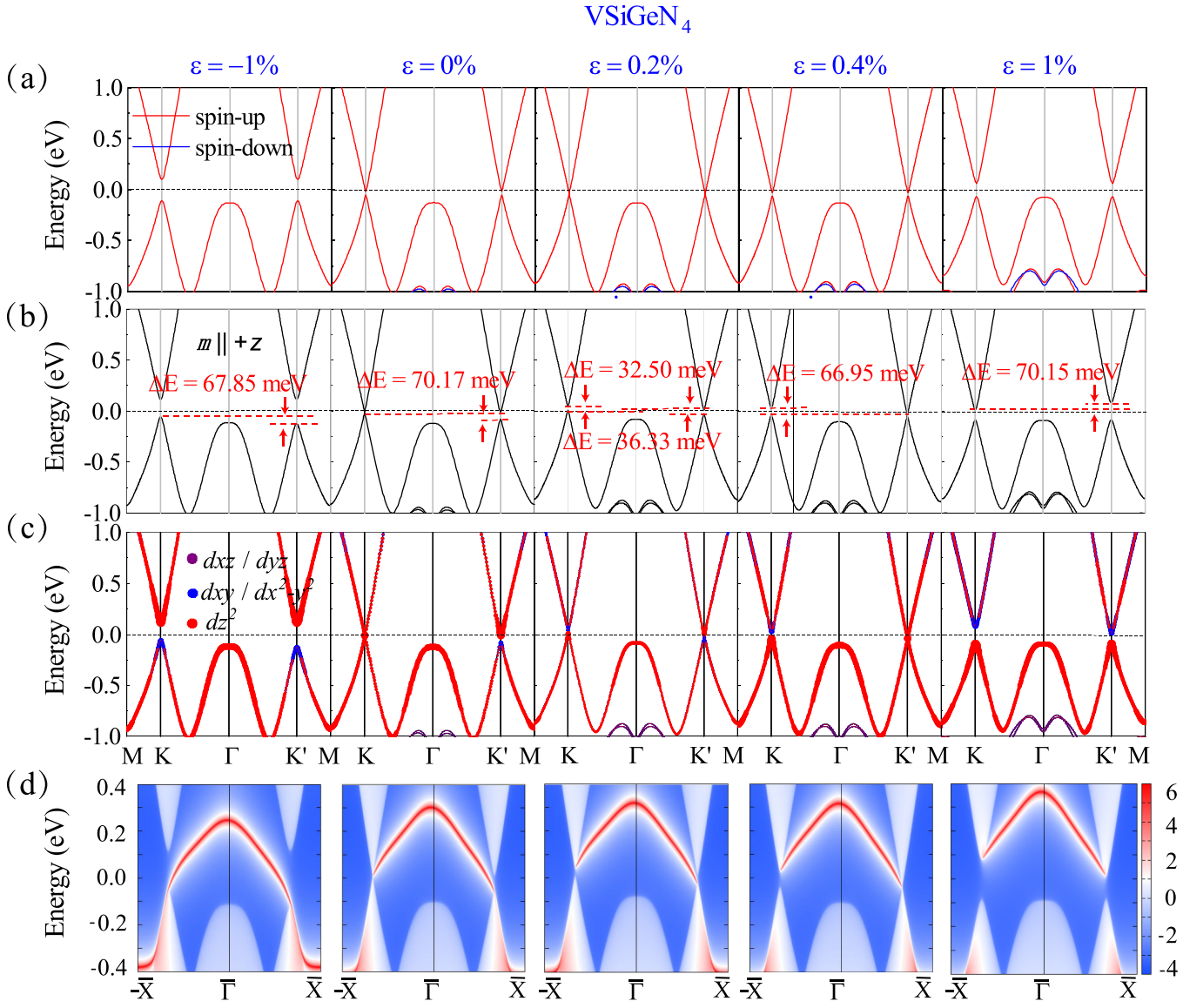

FIG. 5. Band structures and edge state of VSiXN$_4$ monolayer obtained with the GGA + U (U_{eff} = 3 eV) method. (a) Spin-polarized band structures of VSiGeN$_4$ monolayer with the biaxial strain. The red and blue lines represent spin-up and spin-down bands, respectively. (b) Band structure with SOC of VSiGeN$_4$ monolayer with the biaxial strain. (c) Orbital-resolved band structure with SOC of VSiGeN$_4$ monolayer with the biaxial strain. (d) The edge state of VSiGeN$_4$ monolayer with the biaxial strain.

respectively. Then, the valley polarization in the valence and conduction bands can be expressed as

$$E_v^K - E_v^{K'} = i\langle d_{xy}|\hat{H}^0_{\text{SOC}}|d_{x^2-y^2}\rangle - i\langle d_{x^2-y^2}|\hat{H}^0_{\text{SOC}}|d_{xy}\rangle \approx 4\lambda, \tag{10}$$

$$E_c^K - E_c^{K'} = 0, \tag{11}$$

where $\hat{L}_z|d_{xy}\rangle = -2i\hbar|d_{x^2-y^2}\rangle$, $\hat{L}_z|d_{x^2-y^2}\rangle = 2i\hbar|d_{xy}\rangle$. The analytical result indicates that the valley degeneracy splits for the valence and conduction bands are consistent with our DFT calculations ($E_v^K - E_v^{K'} = 70.17$ meV, $E_c^K - E_c^{K'} = 0.00$ meV).

D. Built-in electric-field-induced topological phase transition

To reveal the topological properties of VSiXN$_4$ monolayers, we have calculated the local density of states of the edge state through the Green's function method [43]. As shown in Fig. 3(d), only the VSiGeN$_4$ monolayer exists in a single topologically protected edge state appearing between the conduction and valence bands. This indicates that only VSiGeN$_4$ could be topologically nontrivial, while the others are topologically trivial.

It can be seen that an interesting topological phase transition from VSC to VHSM, to VSC, and to VM appears with the atomic number of X element increasing for the magnetic VSiXN$_4$ monolayers [see Fig. 3(b)]. For instance, the topological phase transition occurs in VSiGeN$_4$ (VHSM). Through a

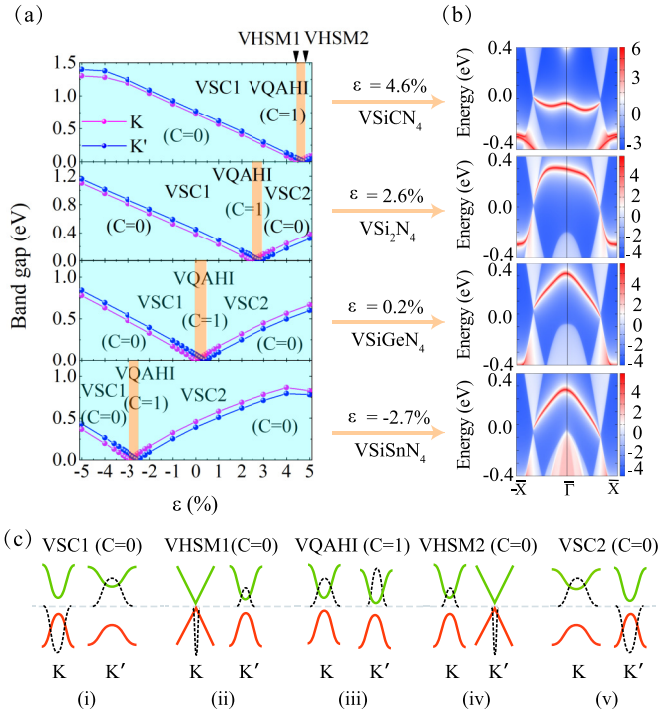

FIG. 6. Band structures and edge state of VSiXN$_4$ monolayer obtained with the GGA + U ($U_{\text{eff}} = 3$ eV) method. (a) The band gap of VSiXN$_4$ at the K and K' points with $-5\% \sim 5\%$ strain, and the orange and light blue shade denotes the VQAHI and VSC states, respectively. (b) The yellow shading corresponds to the edge states. (c) Schematic diagram of the evolution of the band structures and Berry curvatures of VSiXN$_4$ with the various strain. The green solid line, red solid line, and dotted lines represent the valence band, conduction band, and Berry curvatures of VSiXN$_4$ with the various strain, respectively.

detailed analysis of the energy band variation with the atomic number of the X element, it is found that the topological properties are closely related to the gap at the K and K' points. As shown in Fig. 4(a), as the atomic number of X increases, the gap at the K and K' points gradually decreases to zero in VSiGeN$_4$. The fitting curve shows that the band gap at the K and K' points would reach zero when X is Ge, which is the phase-transition point. We further analyzed the built-in electric field, which is caused by the asymmetric Janus structure. Therefore, as shown in Fig. S8, the built-in electric field is defined as $E_{\text{in}} = (\Phi_2 - \Phi_1)/\Delta h$, where Φ_1 and Φ_2 represent the electrostatic potential at the bottom and top of VSiXN$_4$, respectively [33]. The Δh is the structural height of VSiXN$_4$. As shown in Fig. 4(b), more surprisingly, the variation trend of the built-in electric field is completely consistent with the variation trend of the band gap of K and K'. The built-in electric field is 0.36 V/Å (VSiCN$_4$), 0.00 V/Å (VSi$_2$N$_4$), 0.16 V/Å (VSiGeN$_4$), 0.26 V/Å (VSiSnN$_4$), and 0.31 V/Å (VSiPbN$_4$), respectively. This means that the built-in electric field induces a topological phase transition. To prove this, we analyzed the energy level assignments of V-d orbitals for VSiGeN$_4$ and VSiSnN$_4$, as shown in Figs. 4(c) and 4(d). Seeing is believing. It is a band inversion between $d_{xy}/d_{x^2-y^2}$ and d_{z^2} orbitals at the K and K' points in VSiSnN$_4$. Note the built-in electric field introduced by the element, which does not change continuously. VSiGeN$_4$ is the critical point, thus only VSiGeN$_4$ is topologically nontrivial. The continuous variation of the built-in electric field will be described in detail below. In addition, it is well known that applied electric fields can tune the band gap, magnetic ground state, topological properties, and so on. In previous reports [44,45], the electric field is an effective method to tune the topological phase transition. The intrinsic built-in electric field that tunes the topological phase transition is rarely reported.

E. Strain-induced topological phase transition

For a 2D material, its electronic structure can be generally tuned effectively by strain [46–48]. In the following, we investigate the effect of biaxial strain on the spin, valley, and topological properties of VSiXN$_4$. Here, we focus on one representative VSiGeN$_4$. In the calculations, the biaxial strain is defined as $\varepsilon = (a - a_0)/a_0 \times 100\%$. In the formula, a and a_0 represent a lattice constant after and before in-plane biaxial strain is applied, respectively. As shown in Figs. 5(a)–5(c), by increasing strain within a reasonable range ($-5\% \sim 5\%$), when $\varepsilon < 0\%$, the material enters into a VSC. While $\varepsilon = 0\%$, the band gap at the K point is first closed, meanwhile the band gap decreases to 70.17 meV at the K' point. Hence, the VHSM states are acquired in the material. When employ the tensile strain, the band gap at the K point reopens. At the other critical case with $\varepsilon = 0.4\%$, the band gap of the K' point recloses, and the valleys at K' become a Dirac cone-shaped linear dispersion. By continuing to apply the tensile strain to 0.4%, the band gap at the K' point reopens, and it again becomes a VSC.

To understand the mechanism of multiple topological phase transitions, we analyze the orbital-projected band structures and Berry curvature. As shown in Fig. 5(c) and Fig. S9, the compressive strain is 1%, the VBM is dominated by the d_{xy} and $d_{x^2-y^2}$ orbitals of V atoms, while the CBM mainly comes from the d_{z^2} orbital [33]. The Berry curvatures at K and K' have opposite signs. More interestingly, the tensile strain is used (0.2% tensile strain is shown in Fig. 5), and the band gap of the K point reopens. The band inversion occurs between $d_{xy}/d_{x^2-y^2}$ and d_{z^2} orbitals at the K point, while the orbital order does not change at the K' point. Surprisingly, the Berry curvature of K and K' becomes of the same sign. This is a characteristic of VQAHI. It is also confirmed by the calculation of edge states [see Fig. 5(d)]. After the band gap at K' is closed ($\varepsilon = 0.4\%$), by continuing to apply the tensile strain, there is also a band inversion between $d_{xy}/d_{x^2-y^2}$ and d_{z^2} orbitals at the K' point. The signs of the Berry curvatures around the K' flip. Thus, the system returns once again to the VSC.

To further demonstrate the universality of the strain-induced band inversion mechanism in the VSiXN$_4$ system, we systematically investigated the topological properties of VSiXN$_4$ under different strains (band structure shown in Figs. S10–S14) [33]. As shown in Figs. 6(a) and 6(b), it is found that the strain can induce band inversions, which lead to the topological phase transition in these systems. Note that the range of the VQAHI states is different in VSiCN$_4$ (4.5–4.8 %), VSi$_2$N$_4$ (2.5–2.9 %), VSiGeN4 (0.0–0.4 %), and

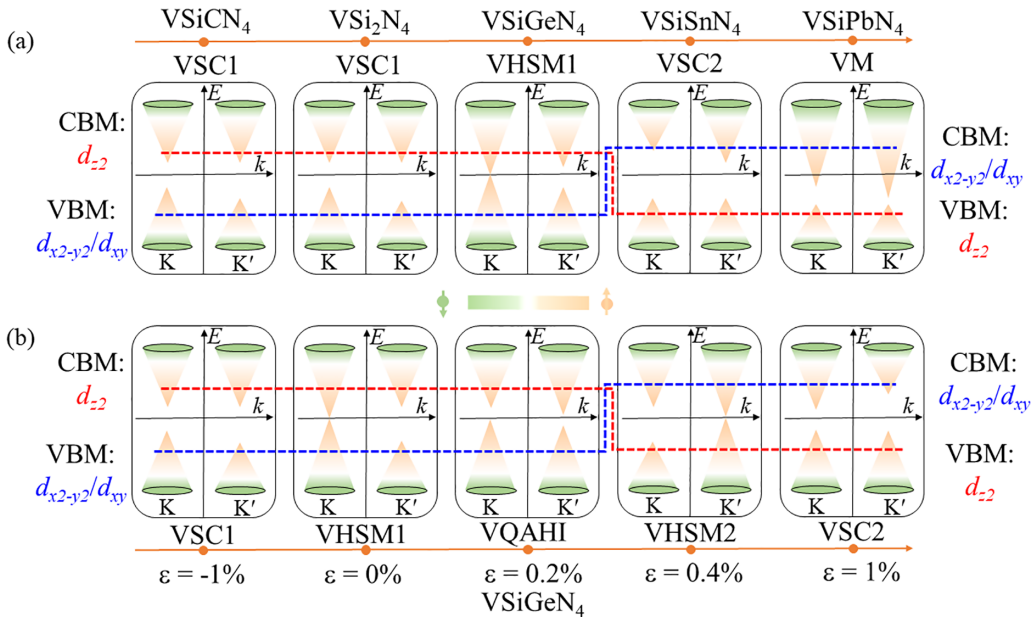

FIG. 7. Schematic diagrams of valley-dependent topological phase transitions. (a) Schematic diagram of the evolution of the band structures with the atomic number of X element increasing for VSiXN$_4$ monolayers. (b) Schematic diagram of the evolution of the band structures for the VSiGeN$_4$ monolayer as a function of strain. These results were obtained with $U_{\text{eff}} = 3$ eV.

VSiSnN$_4$ (-2.9% to 2.5%). To facilitate the reader's understanding, we also provide a table, as listed in Table SII [33]. Most important of all, the valley-related multiple topological phase transitions originate from the change of the sign of the Berry curvatures at the K and K' points. How the band gaps and the topological phase vary with the various strains for the VSiXN$_4$ monolayers is summarized in Fig. 6(c). It is found that the strain magnitude required to achieve topological phase transition is highly dependent on the built-in electric field. We also found that the strain can effectively tune the built-in electric field, and then it induces the band inversion to realize the topological phase transition. In addition, we calculated the results for different U values, as shown in Fig. S15 [33]. When U_{eff} is 1 and 2 eV, the VSiXN$_4$ system does not have topological properties, while when U_{eff} increases to 3 and 4 eV, the VSiXN$_4$ system will create the topological phase with the built-in electric field and strain. Therefore, the band structures vary with the built-in electric field, and strain for VSiXN$_4$ monolayers is summarized in Fig. 7.

To characterize the valley-contrasting physics in VSiXN$_4$ monolayer, we take the VSiGeN$_4$ of -1% strain as an example. The Berry curvatures $\Omega(\mathbf{k})$ of -1% strain VSiGeN$_4$ in the entire 2D BZ and along the high-symmetry line are shown in Figs. 8(a) and 8(b). Clearly, the Berry curvatures at the K and K' points have opposite signs, showing the typical valley polarization characteristic. By integrating the Berry curvature over the BZ, one can further calculate the AHC. As shown in Fig. 8(c), a valley-polarized Hall conductivity clearly exists in the -1% strain VSiGeN$_4$ monolayer. Specifically, when the Fermi level lies between the VBM or CBM of the K and K' valleys, as denoted by the cyan region, a fully spin- and valley-polarized Hall conductivity is generated. This result confirms the existence of the valley anomalous Hall effect in the -1% strain VSiGeN$_4$ monolayer. Moreover, in the hole-doping condition, when the magnetism direction of VSiGeN$_4$ is in the $+z$ direction, the spin-up holes from the K' valley will be generated and accumulate on one boundary of the sample under an in-plane electrical field [upper plane of Fig. 8(d)]. On the other hand, when the magnetism direction is in the $-z$ direction, the spin-up holes from the K valley will be generated and accumulate on the opposite boundary of the sample under an in-plane electrical field [lower plane of Fig. 8(d)]. This feature shows that monolayer VSiGeN$_4$ is an ideal candidate for high-performance valleytronic devices.

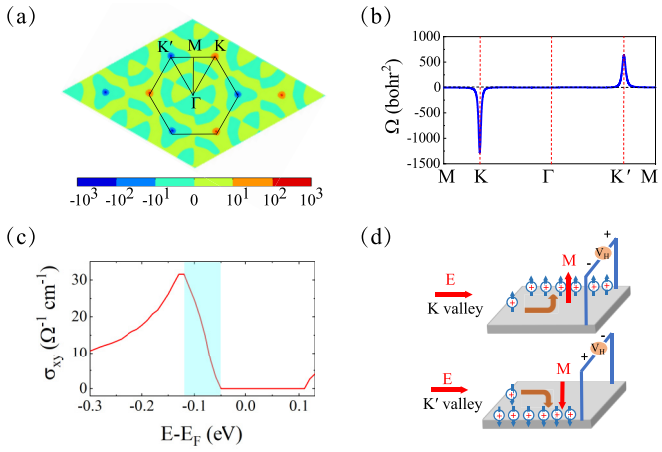

FIG. 8. (a) The Berry curvatures of VSiGeN$_4$ with the strain of -1% in the Brillouin zone and along the high-symmetry line (b). (c) Calculated AHC σ_{xy} as a function of Fermi energy. The light blue shadows denote the valley splitting between the K and K' valley. (d) Schematic diagram of tunable VQAHE in hole-doped VSiGeN$_4$ monolayer at the K and K' valley, respectively. The holes are denoted by the + symbol. Upward and downward arrows refer to spin-up and spin-down carriers, respectively. These results were obtained with $U_{\text{eff}} = 3$ eV.

IV. CONCLUSION

In conclusion, we have demonstrated the rich multifield-induced physics in $VSiXN_4$ (X = C, Si, Ge, Sn, Pn) monolayers. The rich topological phase transitions can be realized through the built-in electric field and strain. Taking the $VSiGeN_4$ monolayer as an instance, when $\varepsilon < 0\%$ and $\varepsilon > 0.4\%$, it is a valley semiconductor. Moreover, the quantum anomalous Hall insulator is obtained with tensile 0.0–0.4 %. At the two critical cases with $\varepsilon = 0.0\%$ and 0.4%, the valleys at K and K', respectively, become a Dirac cone, and the quantum anomalous Hall insulator becomes a valley half-semimetal. We reveal that the nature of the topological phase transition is a built-in electric field, and strain induces band inversion between the $d_{xy}/d_{x^2-y^2}$ and d_{z^2} orbitals at the K and K' valleys. The abundant topological phase transitions make $VSiXN_4$ monolayers a very promising material to develop intriguing spin-valley-topology devices.

ACKNOWLEDGMENTS

This work is supported by the National Natural Science Foundation of China (Grant No. 12004295). P.L. thanks China's Postdoctoral Science Foundation funded project (Grant No. 2022M722547), and the Open Project of State Key Laboratory of Surface Physics (No. KF2022_09). This work was calculated at Supercomputer Center in Suzhou University of Science and Technology.

[1] D. Xiao, W. Yao, and Q. Niu, Valley-Contrasting Physics in Graphene: Magnetic Moment and Topological Transport, Phys. Rev. Lett. **99**, 236809 (2007).

[2] J. R. Schaibley, H. Yu, G. Clark, P. Rivera, J. S. Ross, K. L. Seyler, W. Yao, and X. Xu, Valleytronics in 2D materials, Nat. Rev. Mater. **1**, 16055 (2016).

[3] P. Li, X. Li, W. Zhao, H. Chen, M. X. Chen, Z. X. Guo, J. Feng, X. G. Gong, and A. H. MacDonld, Topological Dirac States beyond π-Orbitals for Silicene on SiC(0001) Surface, Nano Lett. **17**, 6195 (2017).

[4] S. Li, Q. Wang, C. Zhang, P. Guo, and S. A. Yang, Correlation-driven topological and valley states in monolayer VSi_2P_4, Phys. Rev. B **104**, 085149 (2021).

[5] K. Wang, Y. Li, H. Mei, P. Li, and Z. X. Guo, Quantum anomalous Hall and valley quantum anomalous Hall effects in two-dimensional d^0 orbital XY monolayers, Phys. Rev. Mater. **6**, 044202 (2022).

[6] K. Sheng, Q. Chen, H. K. Yuan, and Z. Y. Wang, Monolayer CeI_2: An intrinsic room-temperature ferrovalley semiconductor, Phys. Rev. B **105**, 075304 (2022).

[7] P. Li, X. S. Zhou, and Z. X. Guo, Intriguing magneto-electric effect in two-dimensional ferromagnetic/perovskite oxide ferroelectric heterostructure, npj Comput. Mater. **8**, 20 (2022).

[8] K. F. Mak, K. He, J. Shan, and T. F. Heinz, Control of valley polarization in monolayer MoS_2 by optical helicity, Nat. Nanotechnol. **7**, 494 (2012).

[9] A. Srivastava, M. Sidler, A. V. Allain, D. S. Lembke, A. Kis, and A. Imamoglu, Valley Zeeman effect in elementary optical excitations of monolayer WSe_2, Nat. Phys. **11**, 141 (2015).

[10] J. Zhou, Q. Sun, and P. Jena, Valley-Polarized Quantum Anomalous Hall Effect in Ferrimagnetic Honeycomb Lattices, Phys. Rev. Lett. **119**, 046403 (2017).

[11] X. Feng, X. Xu, Z. He, R. Peng, Y. Dai, B. Huang, and Y. Ma, Valley-related multiple Hall effect in monolayer VSi_2P_4, Phys. Rev. B **104**, 075421 (2021).

[12] X. Zhou, R. W. Zhang, Z. Zhang, W. Feng, Y. Mokrousov, and Y. Yao, Sign-reversible valley-dependent Berry phase effects in 2D valley-half-semiconductors, npj Comput Mater **7**, 160 (2021).

[13] W. Y. Tong, S. J. Gong, X. Wan, and C. G. Duan, Concepts of ferrovalley material and anomalous valley Hall effect, Nat. Commun. **7**, 13612 (2016).

[14] Y. L. Hong, Z. Liu, L. Wang, T. Zhou, W. Ma, C. Xu, S. Feng, L. Chen, M. L. Chen, D. M. Sun *et al.*, Chemical vapor deposition of layered two-dimensional $MoSi_2N_4$ materials, Science **369**, 670 (2020).

[15] L. Wang, Y. Shi, M. Liu, A. Zhang, Y.-L. Hong, R. Li, Q. Gao, M. Chen, W. Ren, H. M. Cheng *et al.*, Intercalated architecture of MA_2Z_4 family layered van der Waals materials with emerging topological, magnetic and superconducting properties, Nat. Commun. **12**, 2361 (2021).

[16] Q. R. Cui, Y. M. Zhu, J. H. Liang, P. Cui, and H. X. Yang, Spin-valley coupling in a two-dimensional VSi_2N_4 monolayer, Phys. Rev. B **103**, 085421 (2021).

[17] C. Yang, Z. Song, X. Sun, and J. Lu, Valley pseudospin in monolayer $MoSi_2N_4$ and $MoSi_2As_4$, Phys. Rev. B **103**, 035308 (2021).

[18] J. Huang, P. Li, X. Ren, and Z. X. Guo, Promising Properties of a Sub-5-nm Monolayer $MoSi_2N_4$ Transistor, Phys. Rev. Appl. **16**, 044022 (2021).

[19] H. Zhong, W. Xiong, P. Lv, J. Yu, and S. Yuan, Strain-induced semiconductor to metal transition in MA_2Z_4 bilayers (M = Ti, Cr, Mo; A = Si; Z = N, P), Phys. Rev. B **103**, 085124 (2021).

[20] Y. T. Ren, L. Hu, Y. T. Chen, Y. J. Hu, J. L. Wang, P. L. Gong, H. Zhang, L. Huang, and X. Q. Shi, Two-dimensional MSi_2N_4 monolayers and van der Waals heterostructures: Promising spintronic properties and band alignments, Phys. Rev. Mater. **6**, 064006 (2022).

[21] A. Y. Lu, H. Zhu, J. Xiao, C. P. Chuu, Y. Han, M. H. Chiu, C. C. Cheng, C. W. Yang, K. H. Wei, Y. Yang *et al.*, Janus monolayers of transition metal dichalcogenides, Nat. Nanotechnol. **12**, 744 (2017).

[22] G. Kresse and J. Hafner, *Ab initio* molecular dynamics for liquid metals, Phys. Rev. B **47**, 558 (1993).

[23] G. Kresse and J. Furthmuller, Efficient iterative schemes for *ab initio* total-energy calculations using a plane-wave basis set, Phys. Rev. B **54**, 11169 (1996).

[24] G. Kresse and D. Joubert, From ultrasoft pseudopotentials to the projector augmented-wave method, Phys. Rev. B **59**, 1758 (1999).

[25] J. P. Perdew, K. Burke, and M. Ernzerhof, Generalized Gradient Approximation Made Simple, Phys. Rev. Lett. **77**, 3865 (1996).

[26] H. L. Zhuang and R. G. Hennig, Stability and magnetism of strongly correlated single-layer VS_2, Phys. Rev. B **93**, 054429 (2016).

[27] A. Togo, F. Oba, and I. Tanaka, First-principles calculations of the ferroelastic transition between rutile-type and $CaCl_2$-type SiO_2 at high pressures, Phys. Rev. B **78**, 134106 (2008).

[28] N. Marzari and D. Vanderbilt, Maximally localized generalized Wannier functions for composite energy bands, Phys. Rev. B **56**, 12847 (1997).

[29] Y. Yao, L. Kleinman, A. H. MacDonald, J. Sinova, T. Jungwirth, D. S. Wang, E. Wang, and Q. Niu, First Principles Calculation of Anomalous Hall Conductivity in Ferromagnetic bcc Fe, Phys. Rev. Lett. **92**, 037204 (2004).

[30] X. Wang, J. Yates, I. Souza, and D. Vanderbilt, *Ab initio* calculation of the anomalous Hall conductivity by Wannier interpolation, Phys. Rev. B **74**, 195118 (2006).

[31] D. J. Thouless, M. Kohmoto, M. P. Nightingale, and M. den Nijs, Quantized Hall Conductance in a Two-Dimensional Periodic Potential, Phys. Rev. Lett. **49**, 405 (1982).

[32] Q. S. Wu, S. N. Zhang, H. F. Song, M. Troyer, and A. A. Suluyanov, WannierTools: An open-source software package for novel topological materials, Comput. Phys. Commun. **224**, 405 (2018).

[33] See Supplemental Material at http://link.aps.org/supplemental/10.1103/PhysRevMaterials.7.064002 for the phonon dispersion curves of the 2H phase (Fig. S1); Fig. S2 shows the lattice structure of the 2H and 1T phase of $VSiXN_4$; Fig. S3 shows the phonon dispersion curves of the 1T phase; Fig. S4 shows the energy difference between AFM and FM spin configurations; Fig. S5 shows the MAE as a function of K-mesh for the $VSiPbN_4$ monolayer; Fig. S6 shows the strain-free band structures of $VSiGeN_4$ and $VSiSnN_4$; Fig. S7 shows the band structures and edge states with the HSE06 method; Fig. S8 shows the planar averaged electrostatic potential; Fig. S9 shows Berry curvature of the various strain $VSiGeN_4$; Figs. S10–S14 show the band structures under various in-plane strains; Fig. S15 shows the band gap of different U values at K and K' under various in-plane strains; Table SI shows the formation energy for 2H and 1T phases $VSiXN_4$ monolayer; Table SII shows the Chern number before and after inducing the built-in electric field and strain.

[34] S. Cahangirov, M. Topsakal, E. Akturk, H. Sahin, and S. Ciraci, Two- and One-Dimensional Honeycomb Structures of Silicon and Germanium, Phys. Rev. Lett. **102**, 236804 (2009).

[35] W. Luo and H. Xiang, Two-dimensional phosphorus oxides as energy and information materials, Angew. Chem. Int. Ed. **55**, 8575 (2016).

[36] B. Goodenough, Theory of the role of covalence in the perovskite-type manganites [La, M(II)]MnO_3, Phys. Rev. **100**, 564 (1955).

[37] J. Kanamori, Superexchange interaction and symmetry properties of electron orbitals, J. Phys. Chem. Solids **10**, 87 (1959).

[38] P. W. Anderson, New approach to the theory of superexchange interactions, Phys. Rev. **115**, 2 (1959).

[39] J. L. Lado and J. F. Rossier, On the origin of magnetic anisotropy in two dimensional CrI_3, 2D Mater. **4**, 035002 (2017).

[40] D. Wang and R. Wu, First-principles theory of surface magnetocrystalline anisotropy and the diatomic-pair model, Phys. Rev. B **47**, 14932 (1993).

[41] J. Hu and R. Wu, Control of the Magnetism and Magnetic Anisotropy of a Single-Molecule Magnet with an Electric Field, Phys. Rev. Lett. **110**, 097202 (2013).

[42] J. Kim, K. W. Kim, B. Kim, C. J. Kang, D. Shin, S. L. Lee, B. C. Min, and N. Park, Exploitable magnetic anisotropy of the two-dimensional magnet CrI_3, Nano Lett. **20**, 929 (2020).

[43] M. P. L. Sancho, J. M. Lopez Sancho, J. M. Lopez Sancho, and J. Rubio, Highly convergent schemes for the calculation of bulk and surface Green functions, J. Phys. F **15**, 851 (1985).

[44] Q. Liu, X. Zhang, L. B. Abdalla, A. Fazzio, and A. Zunger, Switching a normal insulator into a topological insulator via electric field with application to phosphorene, Nano Lett. **15**, 1222 (2015).

[45] X. Li, F. Liu, and Q. Wang, Na-functionalized $IrTe_2$ monolayer: Suppressed charge ordering and electric field tuned topological phase transition, Phys. Rev. B **102**, 195420 (2020).

[46] P. Li and T. Y. Cai, Fully spin-polarized quadratic non-Dirac bands realized quantum anomalous Hall effect, Phys. Chem. Chem. Phys. **22**, 549 (2020).

[47] P. Li and T. Y. Cai, Two-dimensional transition-metal oxides Mn_2O_3 realized the quantum anomalous hall effect, J. Phys. Chem. C **124**, 12705 (2020).

[48] P. Li, Y. Ma, Y. Zhang, and Z. X. Guo, Room temperature quantum anomalous hall insulator in a honeycomb-kagome lattice, Ta_2O_3, with huge magnetic anisotropy energy, ACS Appl. Electron. Mater. **3**, 1826 (2021).